Carbon-slurry optimization for lithium-ion batteries customization

D.C. Orozco-Gallo [*], F.A. Vásquez-Arroyave, J.A. Calderón-Gutierréz [*]

Centro de Investigación, Innovación y Desarrollo de Materiales – CIDEMAT, Universidad de Antioquia., Street 70 N# 52 – 21, Medellín, Colombia

ARTICLE INFO

ABSTRACT

The technological application of lithium-ion batteries (LIB) grows constantly, making customization of the batteries a current necessity and sometimes a challenge. In this paper we described carbon-slurry optimization process for anodes of lithium-ion batteries customization by using a surface response statistical experiment with four response variables such specific discharge capacity, coulombic efficiency, anodes mass deviation, and capacity retention. We studied two commercial graphite active materials by characterizing the materials via Raman spectroscopy, SEM, and electrochemical techniques. We corroborate the graphite structure for both materials but with morphological differences such as shape and particle size. The binder composition seems to interfere with the active carbon materials capabilities while it generates better performance for one of them. Although the chemical structure of both materials was confirmed to be the same via Raman experiments, SEM images shows critical morphological differences that interferes with the final slurry thus, affecting the electrochemical performance of the anodes. Further studies are required to understand ECSA and its possible effect on the charge/discharge capacities of the anodes.

1. Introduction

Energy challenges due to fossil fuels pollution and climate change has accelerate the development of electrochemical power devices to couple renewable sources such as solar and wind to the grid as well as towards cleaner transportation vehicles to help pollution decrease. To achieve such goals, innovative alternative materials are essential for batteries to reach high volumetric and gravimetric energy densities, long cycle life, and safety requirements. Lithium-ion batteries (LIB) are the preferred technology due to their high energy density, lightweight design, and relatively long lifespan compared to other battery chemistries [1–5]. Nowadays, the usage of LIB has been expanded largely into various devices such as robots, power tools, stationary power storage units, uninterrupted power supply (UPS) units, and electrical vehicles (hybrid, plug-in or pure EVs). Unfortunately, conventional Li-ion battery technologies completely fail to meet all the requirement for these applications [1].

The challenges towards lithium batteries focus on lowering the constituent material and manufacturing costs and improving their performance. Among many anode chemistries used in lithium-ion batteries, graphite-based materials are the majority due to its high mechanical strength, electrical and thermal conductivity, and low cost. [5]. The basic arrangement of carbonaceous materials used in LIBs consists of a flat sheet of carbon atoms arranged in a honeycomb structure called graphene. These sheets of carbon stack up in an orderly or disorderly manner to form crystallites. Carbon materials can be classified into soft carbon (graphitic carbon), hard carbon (disordered carbon), and nano-structured carbon. Lithium ions can be intercalated in most of them; however, commercial batteries mainly use the first two types, while the third type is still a matter of study and developing. Graphitic carbons have large graphite grains and can achieve a charge capacity close to theoretical (372 mAh g^{-1}). However, graphitic carbons do not combine well with the propylene carbonate (PC)-based electrolyte, which is the most used in LIBs due to its low melting point and rapid Li$^+$ transport. It has been reported that PC is inserted together with the Li$^+$ between the graphitic planes, causing the graphite to exfoliate and lose capacity [6]. During Li$^+$ intercalation, single-crystalline graphitic particles undergo a 10% uniaxial strain along the edge planes. Such a large strain can damage the "*solid electrolyte interphase*" (SEI) and reduce the life cycle of the cell [7]. On the other hand, hard carbons have small, disorderly oriented graphitic grains and are much less susceptible to exfoliation and cleavage. These grains also have nanogaps between them, resulting in reduced and isotropic volume expansion when Li$^+$ ions enter the structure. Nano voids and defects also provide gravimetric excess capacity, allowing for higher capacity than the theoretical [8]. Mild oxidation of graphite by air leads to the formation of nanochannels with

---

openings of a few nanometers and up to tens of nanometers. These nanochannels were suggested to form on the zigzag and armchair edges between two adjacent crystallites that offer a reversible capacity of up to 405 mAh g^{-1} [8].

The anodic slurry for the main current commercial LIB is a particulate system which typically consists of soft/hard graphite or carbon black as a particle, polyvinylidene difluoride (PVDF) or carboxymethyl cellulose (CMC) and styrene butadiene rubber (SBR) as a binder, and organic or aqueous medium as a solvent. A variety of microstructure in a particulate system can be formed due to the interaction between the particle and polymer such as bridging, depletion attraction or electrostatic repulsion. These structural changes influence the film adhesion and solidification, drying time, and it affects the battery performance [2, 9].

For aqueous anode slurries Carboxymethyl cellulose (CMC) and styrene butadiene rubber (SBR) are often combined as additives to achieve high stability, processability and electrochemical cell performance [10]. Rheological properties of the anode slurries strongly depend on morphology and concentration of the binders where CMC adsorbed preferentially on graphite, dispersing the particles, and stabilizing the slurry resulting in longer cycle life and improved electrochemical cell performance using low substituted CMC [2]. Moreover, polymeric binders on particle dispersion influence the electrical conductivity of electrode layers and it leads to the formation of conducting networks that improve the electron transport kinetics thus, resulting in higher energy, power, and lifetime performance [2,11–13]. Understanding the intrinsic relationship of the binder's composition and interaction between particles highlighted the importance role of increasing the discharge capacity of the electrodes by optimizing the ratios between component that will allow us to achieve higher energy and lifetime performance.

Although the LIB has been developed and commercialized over three decades ago, its technological applications grow constantly, and the customization of the batteries is demanded by the product developers even more. So, traditional coin, prismatic, and 18650 cylindrical cells are not always welcome to the customer. Custom LIBs have been the demand of more and more product vendors, but general product companies lack battery engineers, battery design, and other capabilities. Therefore, small, specialized LIB factories come to help customize the needs of technology products developers. Battery customization, is based on the specific needs of customers to assess a new battery model, considering the technological requirements. Customization of a battery will base on the five major requirements provided by the user, such as: (i) size and shape, (ii) capacity, (iii) C-rate, (iv) temperature-base, (v) voltage-base. All these requirements involve active materials and electrodes development and optimization for LIBs with better performance according to customer's requirements.

In this paper, we focus on the carbon-slurry optimization to obtain the graphitic-base negative electrodes, via doctor blade process. Binder to graphite ratios have been analyzed for two commercial graphite to obtain the highest discharge capacity by increasing the amount of active material in the anode merge with proper rheological properties through a Box-Behnken factorial design to find the optimum combination. Particularly, we studied the changes in film adhesion and solidification on the current collector, mass distribution on the anodes, specific discharge capacity, and coulombic efficiency towards the development of customized cells.

2. Methodology

To obtain the optimal composition ratios, we run a factorial design. Particularly, we applied a Box-Behnken design (BBD) which is a second order response surface method based on three-level incomplete factorial designs for two materials: Graphite Powder Sigma-Aldrich® (C1), and Graphite TMAX-918-III (C2). The special arrangement of the BBD levels allows the number of design points to increase at the same rate as the

Table 1
Box-Behnken experimental design.

Carbon 1/Carbon2			
Variable	Symbol	Levels	
		-1	1
Binder Percentage (%)	Binder	2	4
Thickness of the film (μm)	Thickness	100	200
Carbon Black Super P (%)	Super P	2	4

number of polynomial coefficients. The number of experimental points (N) is obtained by $N = 2k(k-1) + C_0$, where k is the number of variables and C_0 is the number of center points. The factors must be adjusted only at three levels (-1, 0, +1) with equally spaced intervals among them [14]. The total number of experiments run was 13. The factors evaluated were binder percentage, thickness of the applied slurry, and carbon black super P percentage. The response variables evaluated were discharge capacity, coulombic efficiency, and mass standard deviation of the film. Table 1 summarizes the statistical experiment design for each graphite material analyzed.

2.1. Slurry preparation

To prepare the slurry we heat-treated the graphite at 350°C in an argon atmosphere for three hours to remove water in the active material. Then, we proceed to prepare the slurry by using distiller water as solvent, CMC and SBR as binder, carbon Super P®, and graphite as active material, as Table 1 illustrates.

Water was heated up to 80°C to dissolve the CMC for one hour. Then, we added the SBR and keep the mixture for one hour and a half. Meanwhile, we manually milled in agate mortar the graphite and super P then, they were added to the binders-water mixture for thirty minutes to obtain the final slurry.

2.2. Anode preparation

The obtained slurry was painted into a copper foil sheet (10 μm of thickness) by using doctor blade at different gaps to obtain the thickness illustrated in Table 1. Then, we dried the electrodes at 80°C for 12 h and proceeded to cut the electrodes to measure the mass variation at different points.

2.3. Samples characterization

SEM analysis of the anodes prepared as mentioned above were cut to analyze in an JEOL JSM-6490 LV with a voltage of 20kV. Scattering and Backscattering images were taken to analyze morphology and phases present in the samples. Raman spectra were taken in Horiba Jobin Yvon (Labram HR) Nikon (BX41) microscope, with a laser wavelength of 632 nm, 0.3 D filter, and 50X object. The particle size distribution was analyzed with Image J [15] software by sampling 120 particles and the porosity was calculated with a MATLAB program develop by Arash Rabbani and collaborators by contrasting grayscale image with depth maps of the SEM images [16,17].

2.4. Electrochemical analysis

For the half-cell test, the electrodes were assembled into coin cells (type CR2032) in an argon-filled glove box with water and oxygen contents less than 1 ppm. Lithium foil was used as counter and reference electrode, 1.2M LiPF6 in an ethylene carbonate (EC)-dimethyl carbonate (DMC) mixture (1:2 ratio, by volume) (Tianci, Guangzhou, China) as electrolyte, and Celgard 2400 polypropylene film as separator (16 μm of thickness). The potential ranges for tests of graphite anode were 0.02-2.0 V. C-Rate experiments were conducted between 0.2C to 10C to
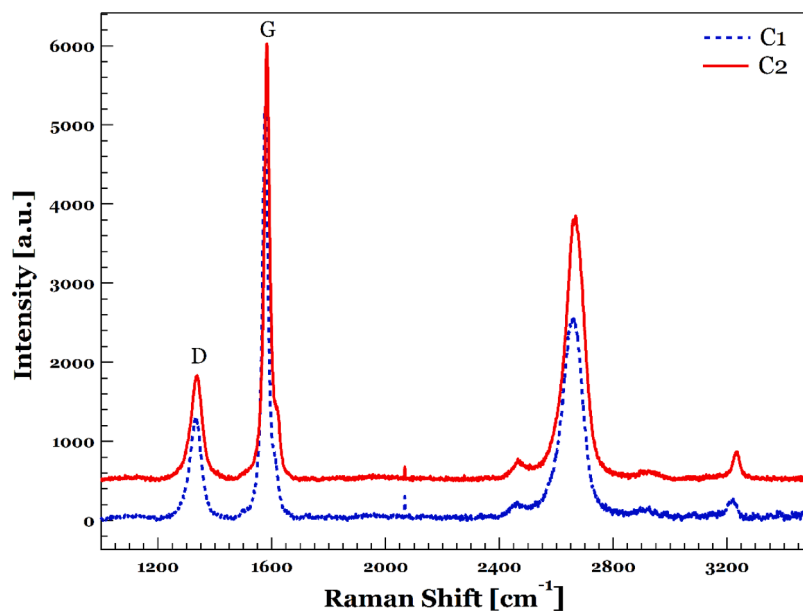
Fig. 1. Raman spectra of graphite samples C1 and C2.

Table 2
Analysis of Variance (ANOVA) for Carbon 1 Discharge Capacity.

Capacity for C1						
Source	Sum of squares	Degrees of freedom	Mean square	F value	P value	Inference
A: Binder Percentage	2.05	1	2.05	0.3	0.6097	Irrelevant
B: Super P Percentage	1046.76	1	1046.76	151.18	0.0001	Significant
C: Thickness μm	7.07	1	7.07	1.02	0.3587	Irrelevant
A^2	509.88	1	509.88	73.64	0.0004	Significant
AB	19.49	1	19.49	2.82	0.1542	Irrelevant
AC	3.35	1	3.35	0.48	0.5178	Irrelevant
B^2	6.01	1	1682,25	0.87	0.3941	Irrelevant
BC	15.84	1	6.01	2.29	0.1908	Irrelevant
C^2	5.62	1	15.84	0.81	0.4089	Irrelevant
Residual	34.62	5	6.92			
R^2	97.89					

evaluate the discharge capacity of the anodes and the capacity retention.

2.5. Rheologic experiments

The flow behavior of the anode slurries was characterized via rotational steady shear measurements with a stress-controlled rheometer (Kinexus Pro+) by running an isothermal shear rate experiment in the range of $10\ Pa < \tau < 2000\ Pa$. All measurements were performed for a 5 min waiting period to ensure structure recovery using a 25mm diameter plate to plate geometry with 1 mm gap, 25°C of temperature, and by applying rotational steady shear.

3. Results and discussion

Fig. 1 shows the Raman spectra of the active materials corroborating the graphite structure for both materials and they do not present any structural difference between them. Typical bands D and G of carbon material appear at around 1326 cm^{-1} and 1570 cm^{-1}, respectively, and are associated with amorphous carbon (D) and graphite carbon (G). The D-band derives from disorder in the sp^2-hybridized carbon, while the G-

Table 3
Analysis of Variance (ANOVA) for Carbon 2 Discharge Capacity.

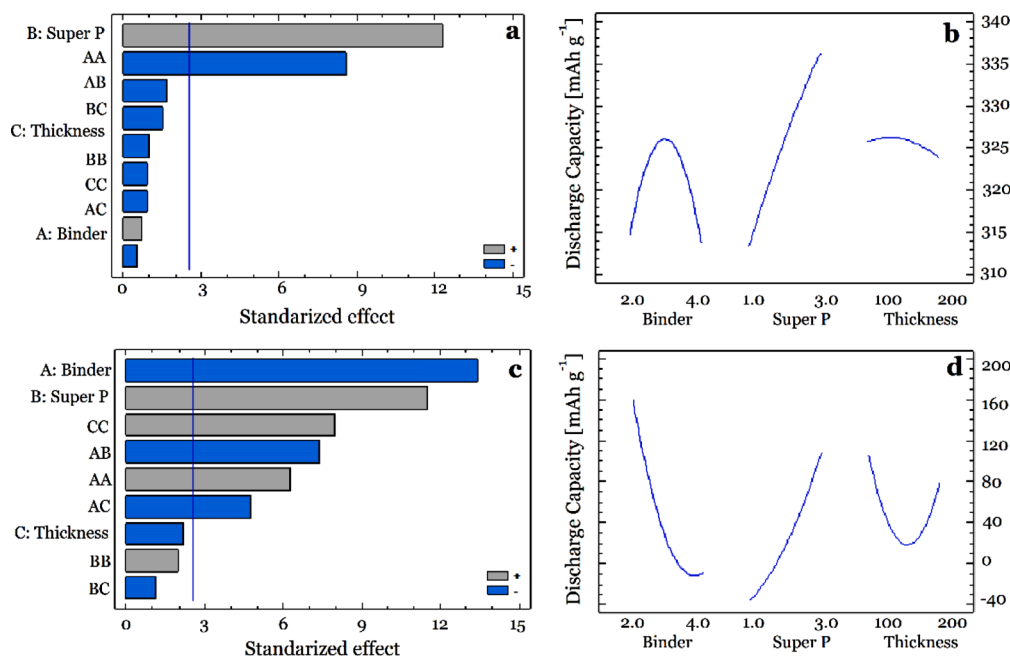| Discharge Capacity C2						
Source	Sum of squares	Degrees of freedom	Mean square	F value	P value	Inference
A: Binder Percentage	56085.7	1	56085.7	179.91	0.0000	Significant
B: Super P Percentage	41164.4	1	41164.4	132.05	0.0001	Significant
C: Thickness μm	1492.76	1	1492.76	4.79	0.0803	Irrelevant
A^2	12217.8	1	12217.8	39.19	0.0015	Significant
AB	16854.5	1	16854.5	54.07	0.0007	Significant
AC	7014.9	1	7014.9	22.5	0.0051	Significant
B^2	1229.6	1	1229.6	3.94	0.1038	Irrelevant
BC	391.8	1	391.8	1.26	0.3132	Irrelevant
C^2	19837.7	1	19837.7	63.63	0.0005	Significant
Residual	1558.7	5	311.74			
R^2	98.99%					

Fig. 2. Statistical analysis on discharge capacity a) Pareto diagram C1, b) Factors effects C1, c) Pareto diagram C2, and d) Factor effects C2.
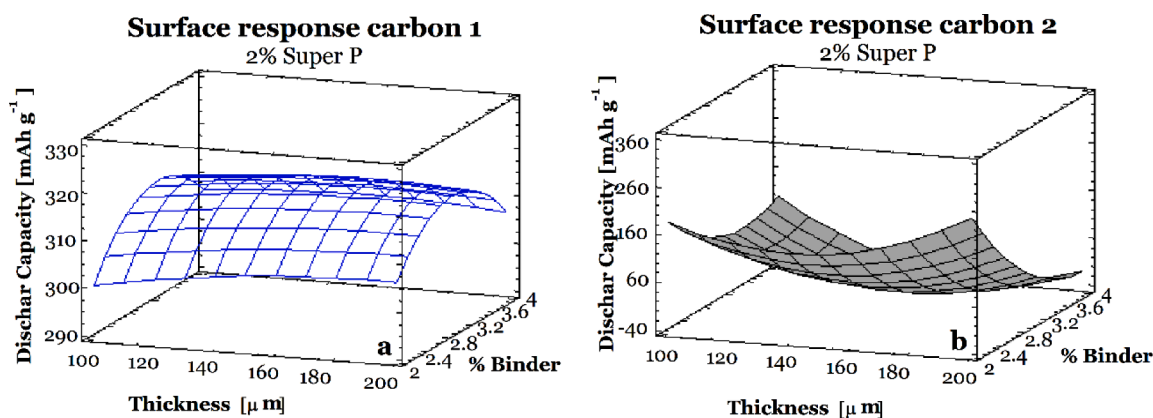

Fig. 3. Surface Response of discharge capacity a) C1 and b) C2.

band is related to the tangential stretching (E2g) mode of graphite [18–20]. The broad-2D band at approx. 2700 cm^{-1} can be related with the second order Raman scattering process [18,21]. The intensity ratio of D-band to G-band (I_D/I_G) give information about the disorder degree of the graphene [22] the I_D/I_G ratio obtained from the Raman spectra of C1 and C2 were 0.2521 cm^{-1} and 0.2353 cm^{-1}, respectively, which suggests that C2 material holds higher graphitization.

The BDD ANOVA results illustrate the main response variables as a function of the factors evaluated as tables 2, 3, and S2-S5 summarized. The design showed us that the coulombic efficiency as well as the mass deviation factors do not correlate directly with the factors evaluated in the selected range (Tables S2-S5). For the coulombic efficiency (Tables S2 and S3), the R^2 is smaller than 84% for both materials and most of the factors are not significant except for the square interaction of the content of carbon black in the sample for C1 (Table S2). Similarly, the mass deviation analysis showed (Tables S4 and S5) R^2 smaller than 82% for both materials and no influence of the factors selected on the variable except the carbon black content for C1 (Table S4).

On the contrary, the discharge capacity response showed a high dependence on the factors selected as the pareto diagram illustrates (Figs. 2a and 2c). For C1 the carbon black content has a positive effect

Table 4
Optimal values for the carbon samples C1 and C2.

C1				C2		
Factor	Low	High	Optimal	Low	High	Optimal
Thickness (µm)	100.0	200.0	100	100,0	200,0	200,0
Binder Percentage	2.0	4.0	2.85	2,0	4,0	2,00004
Super P Percentage	1.0	3.0	3.0	1,0	3,0	2,99857

while the binder interaction has a negative quadratic effect (Fig. 2a) which is better illustrated in the factor effect plot (Fig. 2b). The ANOVA analysis corroborates these results with p-values smaller than 0.05 for factors B and A^2 as Table 2 highlights. Moreover, the surface response obtained (Fig 3a and equation E1) has an R^2 of 97.89% with a well-defined response for the optimization experiment for the evaluated factors. Table 4 summarized the optimal results obtained with 100 µm, 2.85% Binder, and 3.0% carbon black as the values that maximize the discharge capacity of the anode for C1.

Table 5
Summarized selected results of some properties of slurries prepared with graphite samples C1 and C2.

Run C1	Discharge Capacity (mAh g-1)	Porosity	Viscosity (Pa s)	Average particle size (µm)	Run C2	Discharge Capacity (mAh g-1)	Porosity	Viscosity (Pa s)	Average particle size (µm)
E8-100µm	335.52	0.0889	0.4493	9.965	E6-150µm	302.02	0.2213	0.3153	10.703
E8-200µm	330.86	0.1466	0.3483	8.120	E4-200µm	274.69	0.1712	0.2823	11.043
E3-100µm	314.06	0.2787	0.3095	9.471	E8-200µm	158.36	0.2360	0.3753	11.457
E1-150µm	298.97	0.2871	0.1760	7.675	E5-150µm	11.66	0.3596	0.4217	11.198

$$Dis.\ Capacity\ C1 = 168.59 + 71.67A + 29.14B + 0.15C - 11.75A^2$$
$$- 2.21AB + 0.018AC - 1.28B^2 - 0.0398BC$$
$$- 0.00005C^2 \tag{E1}$$

For C2 discharge capacity the factors effects and interactions are stronger than for C1. The binder content, binder/carbon black, and binder/thickness interaction have a negative effect while the carbon black content, thickness, and binder square effects have a positive one (Fig. 2c) which is better illustrated in the factor effect plot (Fig. 2d). The ANOVA analysis corroborates these results with p-values smaller than 0.05 for these A, B, A^2, AB, C^2, and AC as table 3 highlights. Furthermore, the surface obtained (Fig 3b and equation E2) has an R^2 of 98.99% by displaying a minimization response which suggest that factors values were in the wrong range for the design of this material. Table 4 summarized the optimal results obtained with 200 µm, 2% Binder, and 2.99% carbon black as the values that maximize the discharge capacity of the anode for C2.

$$Dis.\ Capacity C2 = 592.16 - 173.41A + 223.17B - 6.16C + 57.523A^2$$
$$- 64.91AB - 0.84AC + 18.25B^2 - 0.20BC + 0.03C^2 \tag{E2}$$

To better understand the results obtained by the BDD experiment we analyzed SEM results which illustrate significant morphological differences in both materials and their effect on the agglomerate and porosity formation during the slurry preparation process. Moreover, to analyze the overall effect, we selected four samples which represented the best anode, second best, intermediate, and lowest performance in terms of discharge capacities as we evidence the importance of the factors from the statistical analysis for this response variable. These material samples results are summarized in Table 5 from the total experimental results presented in Table S1, in the supporting information. Figs. 4 and 5 illustrate significant morphological differences in both materials with flake-like shape for C1 (Fig. 4) and spherical shape for C2(Fig. 5), respectively. These morphological differences might explain the opposite surface behavior obtained in the BDD.

It is important to recall that the particle-binder interaction will reflect on the slurry viscosity and the porosity achieved in the final electrode thus, the morphological differences showed us the difference in the response variables we analyzed. Particularly, film adherence will be reflected in the anodes mass deviation at different points in the film as Table S1 illustrate. For instance, in C1 the smallest mass deviation does not correlate to the binder content as we expected and in agreement with of our statistical analysis by any of the factors evaluated.

However, there is a significant importance in the carbon-binder interaction due to the surface dangling bonds on the solid particle in which the polymers tend to chemically bond or physically absorb to form a 1 to 5 nm polymer layer around it that cannot be dissolved thus, forming the immobilized polymer layer between covered particles, and avoiding the free polymer domains inside the slurry.

Fig. 4a and 4d illustrate the agglomeration of particles where the slurries with intermediate binder content form a more distributed particle size (Fig. 6a and 6b) limited by the immobilized polymer surrounding the particles. It also showed polymer concentrated regions (Fig. 4g) as well as a porosity decrease (Fig. 4b, 4e, 4h, 4k, and Table 5). However, for highest binder concentrations (Fig. 4g) the polymer is capable to form not only immobilized regions but free polymer domains. Furthermore, previous slurries studies [11,23] have showed the carbon black effect on the slurry stability as it is a spherical particle that promotes particles fused during the slurry preparation due to its high surface area.

As ANOVA results for discharge capacity in C1 highlight the positive carbon black effect on the discharge capacity is due to the morphology and surface area differences where flake-like carbon has less surface area than carbon black particles if we compared the average particle size of the flakes for C1 between 7.6 µm to 10 µm (Fig. 6 and Table 5) and
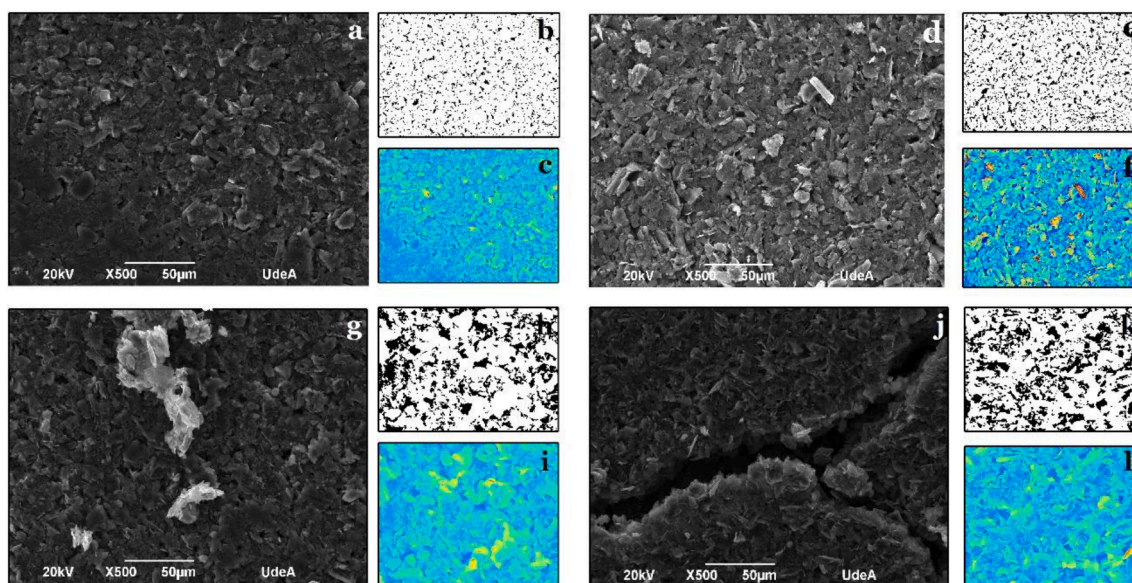
Fig. 4. Carbon 1 SEM analysis organized in performance order from highest to lowest. a) Anode slurry Experiment 8, b) Binary Segmentation Experiment 8, c) Depth Map Experiment 8, d) Anode slurry Experiment 7, e) Binary Segmentation Experiment 7, f) Depth Map Experiment 7, g) Anode slurry Experiment 3, h) Binary Segmentation Experiment 3, i) Depth Map Experiment 3, j) Anode slurry Experiment 1, k)Binary Segmentation Experiment 1, and l) Depth Map Experiment 1.
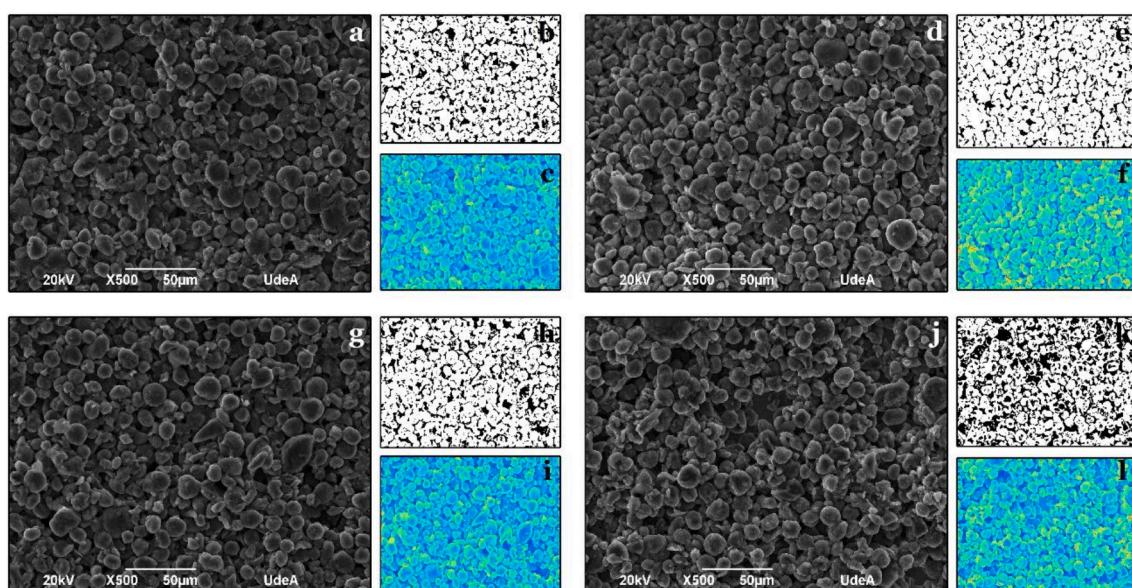

Fig. 5. Carbon 2 SEM analysis organized in performance order from highest to lowest. a) Anode slurry Experiment 6, b) Binary Segmentation Experiment 6, c) Depth Map Experiment 6, d) Anode slurry Experiment 4, e) Binary Segmentation Experiment 4, f) Depth Map Experiment 4, g) Anode slurry Experiment 8, h) Binary Segmentation Experiment 8, i) Depth Map Experiment 8, j) Anode slurry Experiment 5, k) Binary Segmentation Experiment 5, and l) Depth Map Experiment 5.

carbon black particles sizes reported are smaller than 500 nm. Furthermore, carbon black particles have low percolation threshold when combined in a polymer composite thus, the ratio binder/carbon black directly affects the electronic conductivity of the slurry and as consequence, increases not only the discharge capacity but also the coulombic efficiency.

Moreover, the highest coulombic efficiencies were achieved with highest super conductive carbon which seems to have a better interaction with the binder and thus, help to achieve better adhesion of the film. In terms of discharge capacity, the binder effect seems to be negative at lowest and higher values. In the first case, the lowest content of binder generates worse adhesion which is evident in the SEM images (Fig. 4j) by generating less particle-particle adhesion, bigger fractures at lower scales, and lower porosities (E1-150μm Table 5 and Fig. S1). On the

contrary, middle binder contents seems to stabilize the slurry and generates a more uniform film with lower porosity (E8-100μm Table 5 and Fig. S1) thus, increasing the discharge capacity of the anode.

ANOVA results for discharge capacity in C2 not only remarks the carbon black positive effect on the discharge capacity but also the cross-interaction effects related to carbon black/binder interaction. For this type of carbon, we have the same morphology than for carbon Super P thus, the smaller particle size help with the formation of immobilized polymer region and decreases the amount of free polymer to create the composite. As consequence, the particle seems more defined in the SEM images (Fig. 5) with polymer coverage more defined and without the presence of free polymer areas.

Moreover, the porosity and average particle size values for these slurries (Table 5 and Fig. 7) are higher than for C1 as the free polymer
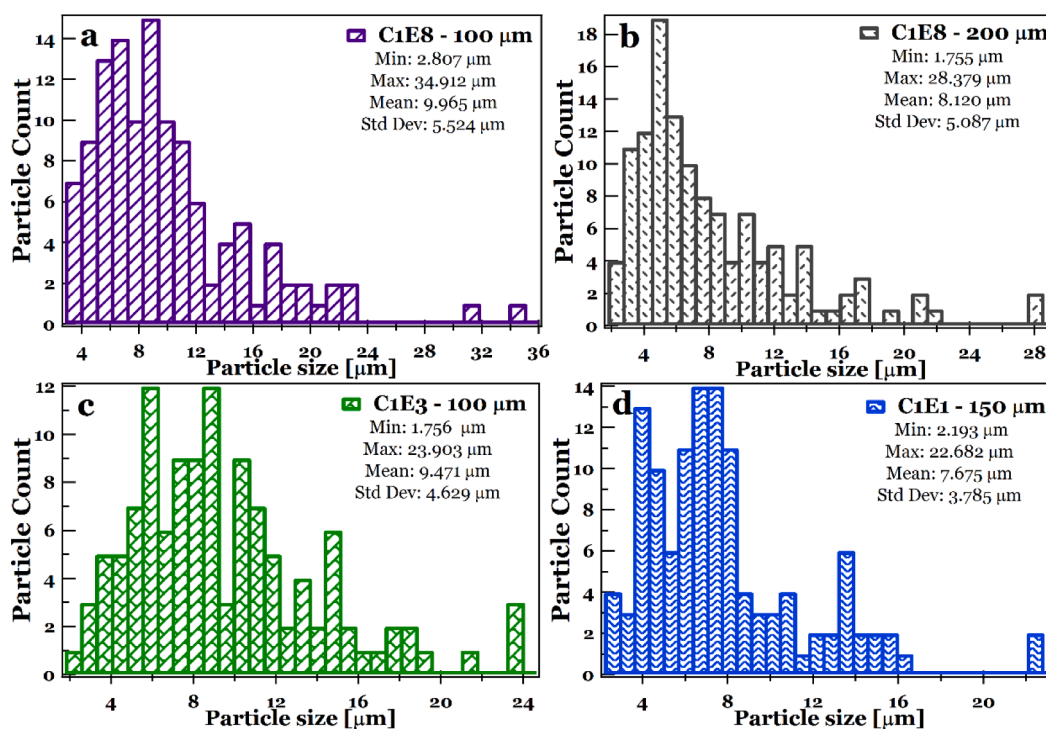
Fig. 6. Carbon 1 Particle Size Distribution in performance order from best to worse: a) C1E8-100μm, b) C1E7 150μm, c) C1E3 100 μm, and d) C1E1 150μm.

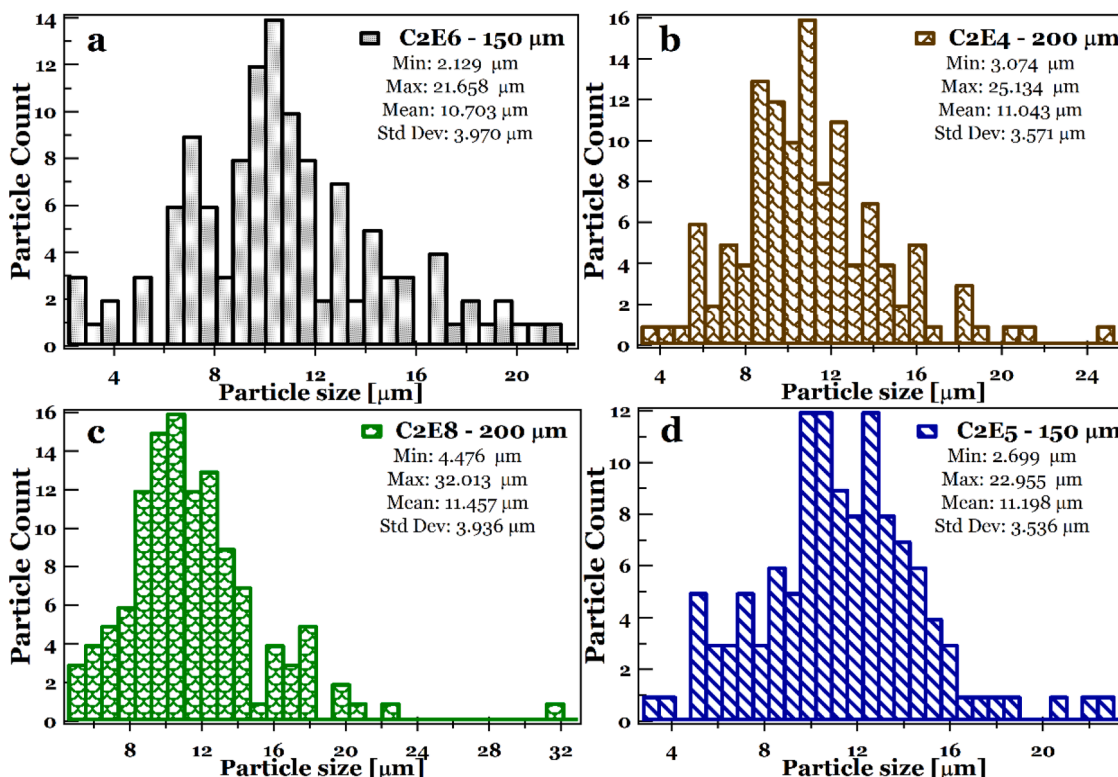**Fig. 7.** Carbon 2 Particle Size Distribution in performance order from best to worse a) C2E6-150μm, b) C2E4 - 200μm, c) C2E8 - 200 μm, and d) C2E5 - 150μm.

availability decreases and more dispersed slurries are obtained. Thus, the negative binder and binder/carbon black interactions and its reflection on the SEM analysis agree with our statistical findings. Besides, the lowest content of binder generates less adhesion with is evident in the SEM images (Fig. 5j) which more polymer covered particles and lower porosities (E5-150μm Table 5 and Fig. S2). On the

contrary, middle to higher binder contents seems to stabilize the slurry and generates a more uniform film with lower porosity (E6-150 μm, E4-200 μm, and E8-200 μm Table 5 and Fig. S2) thus, increasing the discharge capacity of the anode.

Adherence and mass of the electrodes are key features to obtained higher capacities and guarantee longer life cycles. In this sense, the
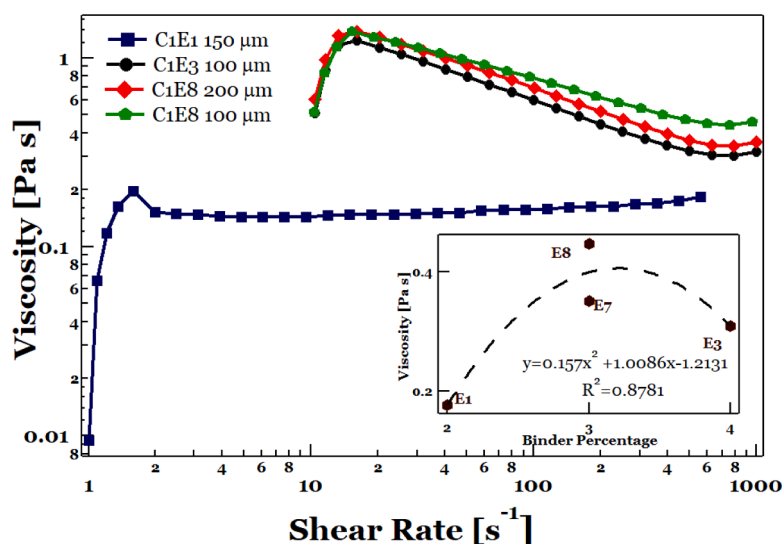
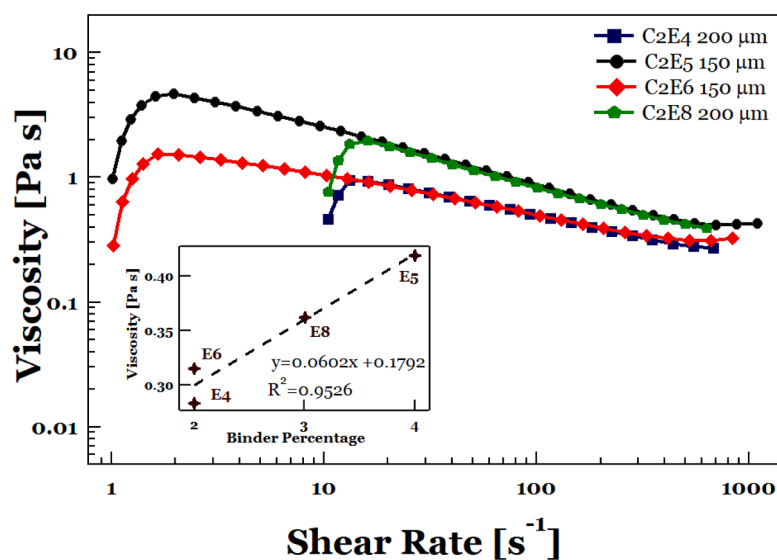**Fig. 8.** Anode slurries viscosity vs. Shear rate for C1.

Fig. 9. Anode slurries viscosity vs. Shear rate for C2.

viscosity of the slurries play an important role to achieve it. We analyzed the viscosity changes as the binder content of the slurries were modified. Fig. 8 illustrates the viscosity and flow changes due to this variation for C1. On one hand, the smaller binder content (2%, C1E1) slurry exhibits a Newtonian-type fluid behavior related with the water as solvent and the curve shows a constant viscosity in a wide range of shear rate which presented more liquid slurries and generates the worse anodes (Fig S1, in the supporting information).

Furthermore, as binder content increases (3% and 4%) the slurries become non-Newtonian (Fig. 8 C1E3 and C1E8) presenting similar behavior. The low shear - viscosity region in the graph indicates incomplete particles dispersion which indicates that some agglomerates are immobilizing the solvent while higher shear stresses reveal agglomerates breaking thus, slurries viscosity matches. As consequence, the viscosity changes with binder content show a maximum viscosity at 3% of content, consistent with the statistical analysis and with the quality of the painted electrodes obtained (Fig. S1, C1E8) where the best adhesion and homogeneous anodes correspond to this binder content.

On the other hand, Fig. 9 illustrates the viscosity and flow changes for C2 which illustrate non-Newtonian behavior for all binder

variations. For the smallest binder contents (2%, C2E6 and C2E4) the lower shear - viscosity region indicates incomplete particles dispersion, but it showed the opposite response from flake-type carbon (C1). This result reveals that for spherical particles is better to immobilizing the solvent with the binder to increase the agglomeration while higher shear stresses reveal that the agglomerates break. Slurries viscosity matches in all cases with a slight increase in viscosity as the binder content rises. As consequence, the viscosity linearly increases with binder content, but it does not reflect on the anode performance, but it is consistent with the statistical analysis. It was observed negative effect of the binder and with the quality of the painted electrodes obtained for lower binder concentrations (Fig. S2, C2E6 and C2E4 in the supporting information) where the best adhesion and homogeneous anodes correspond to lower binder content.

The binder/carbon black interactions influence on the slurry's fluid behavior is related to the amount of fixed polymer surrounding the particles which is a function of the filler particles while flake-like materials (C1) are less porous the polymer coverage remains on the outer expose surface thus, the slurries generate a more condensed structure and more homogeneous anode (Fig. 4a and Fig S1, C1E8-100μm). On the
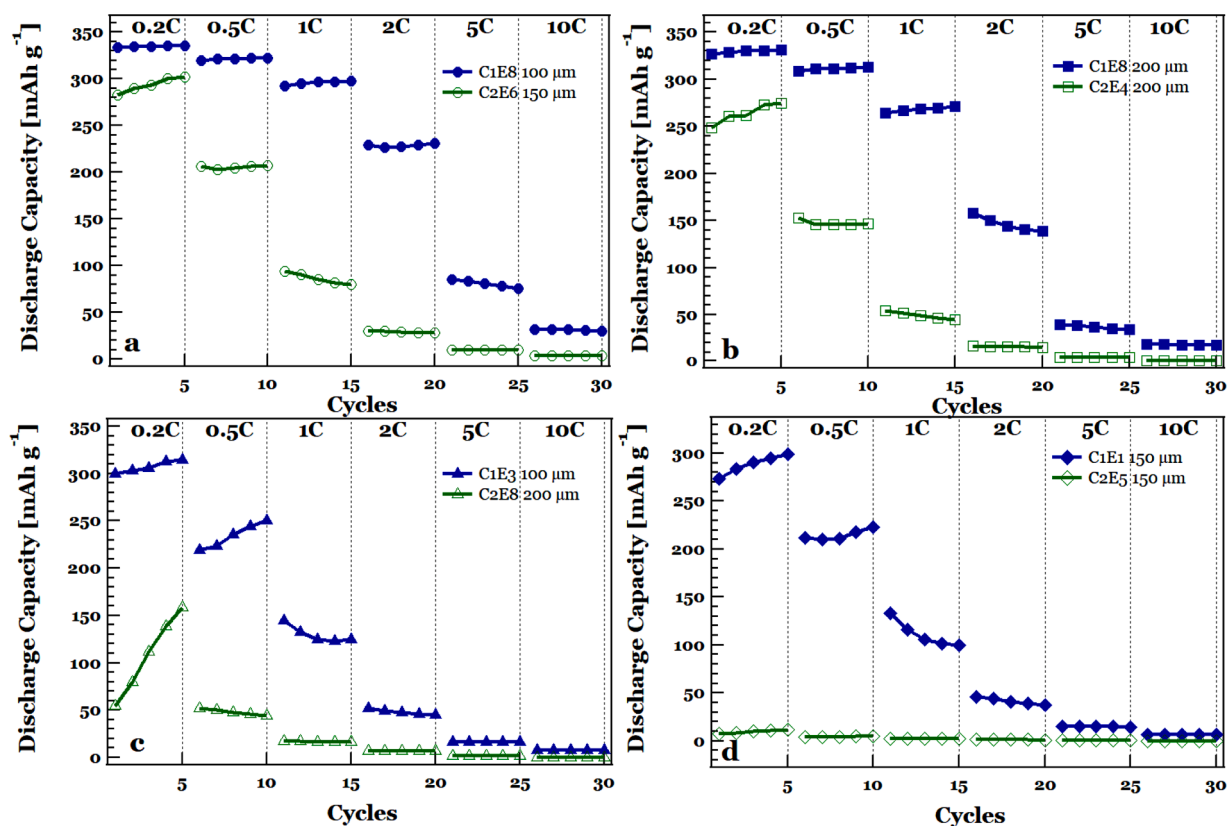
Fig. 10. Discharge Capacity for the graphite evaluated for the best to worse performed materials, filled markers correspond to carbon 1 and empty markers corresponds to carbon 2. a) Higher response b) second best response, c) intermediate response, and d) worse response.

contrary, on spherical particles (C2) the porosity is higher then, the polymer can penetrate and filled the particle therefore, generating a more disperse and more heterogenous anode (Fig. 5j and Fig S2, C2E5). As consequence, these interactions influence the long-ranges anode electronic conductivity where to achieve high energy anodes we aim to increase the active material amount and decrease the binder and carbon black contents.

The electrochemical performance of the anodes was studied at different C-Rates as Fig. 10 illustrates where we contrast both materials from the best performed to the worse. In all cases C1 exhibits the best anode performance with a discharge capacity of 335.52 mAh g^{-1} at 0.2C and coulombic efficiency of 92.3% on the first cycle (Fig. 10a, Table S1 C1E8-100μm) in comparison with 302.02 mAh g^{-1} and 96.2% on the first cycle for C2 (Fig. 10a, Table S1 C2E6-150 μm). Thus, in the best performance cases C1 and C2 exhibited 98.6% and 88.8% of the theoretical capacity, respectively. For the worse performed anodes, the discharge capacity at 0.2C was 298.997 mAh g^{-1} and coulombic efficiency of 90.6% (Fig. 10d, Table S1 C1E1-150 μm) in comparison with 11.66 mAh g^{-1} and 72.9% (Fig. 10d, Table S1 C1E5-150 μm). Furthermore, in all cases C1 anodes exhibited better rate-capability performance than C2 ones. The combined effects of optimizing the binder/carbon black relation as well as the appropriate thickness selection as result of the statistical analysis allowed us to select flake-like carbons as the anodes material for further scaling of the batteries due to its higher discharge capacity and consistent coulombic efficiency reported in Fig. 10 thus, validating the optimization process presented here.

In terms of the lithiation/delithiation processes, compact and less porous electrodes favor the lithium mobility as consequence of the morphological effects mentioned above where the binder increases the particle-particle adhesion thus, generates less tortuous paths for the ions to move. Finally, the discharge capacity increases as a combined effect of the slurry's component interaction, being the binder/active material

and binder/carbon black interactions, the ones dominating the electrochemical performance.

4. Conclusion

An BBD optimization study for graphite anodes slurries was presented to highlight the importance of the component's interactions, particularly the graphite's characteristics, to obtained higher performed anodes of lithium-ion batteries customization. The discharge capacity is the response variable that is most affected by the selected factors while for the efficiency and the mass deviation those factors does not impact the variables response. The carbon black content is the most significant effect in both materials which is reflected in higher capacities and coulombic efficiencies. However, in terms of the overall behavior the binder/carbon black interactions are relevant in terms not only of electrochemical performance but also in the obtention of more homogeneous and better adhesion anodes. The optimal values differ from each graphite material due to its morphological distinctions. Moreover, for flake-like carbon the binder content strongly affects the performance and generates a maximum in the response surface due to the binder/carbon interactions while for spherical carbon the surface response is a minimization suggesting that for this type of materials the selected range for the variables is not appropriate. Although flake-like carbon represents the best performed anode in terms of discharge capacity as well as C-Rate performance for the selected range, spherical carbons can be further explored to find the better range of values due to its superior coulombic efficiency which might represent in the future longer lifetime spam for the battery. Finally, statistical design processes of both materials show us that for scaling anodes up and batteries customization the best material is the flake-like carbon with a binder and carbon black composition of 2.85% and a thickness of 100 μm.

Author Contributions

Diana Orozco: Performing material characterization, electrode preparation and electrochemical measurements, Conceptualization, Methodology, Formal analysis, Writing - Review and Editing. F.A. Vásquez: Sample fabrication, Formal Analysis, Writing - Review. Jorge A. Calderón: Conceptualization, Writing - Review and Editing, Supervision, Project administration.

Declaration of Competing Interest

The authors declare that they have no known competing financial interests or personal relationships that could have appeared to influence the work reported in this paper.

Data availability

Data will be made available on request.

Supplementary materials

Supplementary material associated with this article can be found, in the online version, at doi:10.1016/j.electacta.2023.143141.

References

[1] J. Lu, Z. Chen, F. Pan, Y. Cui, K. Amine, High-Performance Anode Materials for Rechargeable Lithium-Ion Batteries, Electrochem. Energ. Rev. 1 (2018) 35–53, https://doi.org/10.1007/s41918-018-0001-4.

[2] S. Lim, S. Kim, K.H. Ahn, S.J. Lee, The effect of binders on the rheological properties and the microstructure formation of lithium-ion battery anode slurries, J. Power Sources 299 (2015) 221–230, https://doi.org/10.1016/j.jpowsour.2015.09.009.

[3] W.U. YongJian, T. RenHeng, L.I. WenChao, W. Ying, H. Ling, O. LiuZhang, A high-quality aqueous graphene conductive slurry applied in anode of lithium-ion batteries, J. Alloys Compd. 830 (2020), https://doi.org/10.1016/j.jallcom.2020.154575.

[4] C.W. Kwon, S.E. Cheon, J.M. Song, H.T. Kim, K.B. Kim, C.B. Shin, S.W. Kim, Characteristics of a lithium-polymer battery based on a lithium powder anode, n.d.

[5] J. Garofalo, J. Lawler, D. Walczyk, N. Koratkar, Analysis of Deposition Methods for Lithium-Ion Battery Anodes Using Reduced Graphene Oxide Slurries on Copper Foil, J. Manufact. Sci. Eng. Trans. ASME 140 (2018), https://doi.org/10.1115/1.4040265.

[6] D. Aurbach, B. Markovsky, I. Weissman, E. Levi, Y. Ein-Eli, On the correlation between surface chemistry and performance of graphite negative electrodes for Li ion batteries, Electrochim. Acta 45 (1999) 67–86, https://doi.org/10.1016/S0013-4686(99)00194-2.

[7] H. Nozaki, K. Nagaoka, K. Hoshi, N. Ohta, M. Inagaki, Carbon-coated graphite for anode of lithium ion rechargeable batteries: Carbon coating conditions and precursors, J. Power Sources 194 (2009) 486–493, https://doi.org/10.1016/J.JPOWSOUR.2009.05.040.

[8] Perla B Balbuena, Y. Wang, Lithium-ion Batteries: Solid-Electrolyte Interphase, ICP (2004).

[9] S. Jaiser, N. Sanchez Salach, M. Baunach, P. Scharfer, W. Schabel, Impact of drying conditions and wet film properties on adhesion and film solidification of lithium-ion battery anodes, Drying Technology. 35 (2017) 1807–1817. doi:10.1080/07373937.2016.1276584.

[10] R. Gordon, R. Orias, N. Willenbacher, Effect of carboxymethyl cellulose on the flow behavior of lithium-ion battery anode slurries and the electrical as well as mechanical properties of corresponding dry layers, J. Mater. Sci. 55 (2020) 15867–15881, https://doi.org/10.1007/s10853-020-05122-3.

[11] Particles and Polymer Binder Interaction: A Controlling Factor in Lithium-Ion Electrode Performance, (2012). doi:10.1149/2.024203jes.

[12] B. Lestriez, Functions of polymers in composite electrodes of lithium ion batteries, Comptes Rendus Chimie 13 (2010) 1341–1350, https://doi.org/10.1016/J.CRCI.2010.01.018.

[13] D. Guy, B. Lestriez, R. Bouchet, D. Guyomard, Critical Role of Polymeric Binders on the Electronic Transport Properties of Composites Electrode, J. Electrochem. Soc. 153 (2006) A679, https://doi.org/10.1149/1.2168049.

[14] T.J. Robinson, Box-Behnken Designs. Wiley StatsRef: Statistics Reference Online, 2014, https://doi.org/10.1002/9781118445112.stat04101.

[15] C.A. Schneider, W.S. Rasband, K.W. Eliceiri, NIH Image to ImageJ: 25 years of image analysis, Nat. Methods 9 (2012) 671–675, https://doi.org/10.1038/nmeth.2089.

[16] A. Rabbani, S. Salehi, Dynamic modeling of the formation damage and mud cake deposition using filtration theories coupled with SEM image processing, J. Nat. Gas Sci. Eng. 42 (2017) 157–168, https://doi.org/10.1016/J.JNGSE.2017.02.047.

[17] C.P. Ezeakacha, A. Rabbani, S. Salehi, A. Ghalambor, Integrated Image Processing and Computational Techniques to Characterize Formation Damage, in: Proceedings - SPE International Symposium on Formation Damage Control. 2018-February, 2018, https://doi.org/10.2118/189509-MS.

[18] R. Muzyka, S. Drewniak, T. Pustelny, M. Chrubasik, G. Gryglewicz, Characterization of graphite oxide and reduced graphene oxide obtained from different graphite precursors and oxidized by different methods using Raman spectroscopy, Materials 11 (2018) 15–17, https://doi.org/10.3390/ma11071050.

[19] T. Wang, S. Kumar, Electrospinning of polyacrylonitrile nanofibers, J. Appl. Polym. Sci. 102 (2006) 1023–1029, https://doi.org/10.1002/app.24123.

[20] C.A. Velásquez, F.A. Vásquez, M. Alvarez-Láinez, A. Zapata-González, J. A. Calderón, Carbon nanofibers impregnated with Fe3O4 nanoparticles as a flexible and high capacity negative electrode for lithium-ion batteries, J. Alloys Compd. 862 (2021), 158045, https://doi.org/10.1016/j.jallcom.2020.158045.

[21] X.J. Lee, B.Y.Z. Hiew, K.C. Lai, L.Y. Lee, S. Gan, S. Thangalazhy-Gopakumar, S. Rigby, Review on graphene and its derivatives: Synthesis methods and potential industrial implementation, J. Taiwan Inst. Chem. Eng. 98 (2019) 163–180, https://doi.org/10.1016/j.jtice.2018.10.028.

[22] S. Dai, Z. Liu, B. Zhao, J. Zeng, H. Hu, Q. Zhang, D. Chen, C. Qu, D. Dang, M. Liu, A high-performance supercapacitor electrode based on N-doped porous graphene, J. Power Sources 387 (2018) 43–48, https://doi.org/10.1016/j.jpowsour.2018.03.055.

[23] B. Wu, W. Lu, A consistently coupled multiscale mechanical–electrochemical battery model with particle interaction and its validation, J. Mech. Phys. Solids 125 (2019) 89–111, https://doi.org/10.1016/j.jmps.2018.12.005.